J Appl Physiol 92: 835–845, 2002.
First published October 26, 2001; 10.1152/japplphysiol.00385.2001.

Kinematically irreversible acinar flow: a departure from classical dispersive aerosol transport theories

F. S. HENRY,[1] J. P. BUTLER,[2] AND A. TSUDA[2]
[1]*School of Engineering, City University, London EC1V 0HB, United Kingdom; and* [2]*Physiology Program, Harvard School of Public Health, Boston, Massachusetts 02115*

Received 23 April 2001; accepted in final form 22 October 2001

Henry, F. S., J. P. Butler, and A. Tsuda. Kinematically irreversible acinar flow: a departure from classical dispersive aerosol transport theories. *J Appl Physiol* 92: 835–845, 2002. First published October 26, 2001; 10.1152/japplphysiol.00385.2001.—Current theories describe aerosol transport in the lung as a dispersive (diffusion-like) process, characterized by an effective diffusion coefficient in the context of reversible alveolar flow. Our recent experimental data, however, question the validity of these basic assumptions. In this study, we describe the behavior of fluid particles (or bolus) in a realistic, numerical, alveolated duct model with rhythmically expanding walls. We found acinar flow exhibiting multiple saddle points, characteristic of chaotic flow, resulting in substantial flow irreversibility. Computations of axial variance of bolus spreading indicate that the growth of the variance with respect to time is faster than linear, a finding inconsistent with dispersion theory. Lateral behavior of the bolus shows fine-scale, stretch-and-fold striations, exhibiting fractal-like patterns with a fractal dimension of 1.2, which compares well with the fractal dimension of 1.1 observed in our experimental studies performed with rat lungs. We conclude that kinematic irreversibility of acinar flow due to chaotic flow may be the dominant mechanism of aerosol transport deep in the lungs.

lung; deposition; chaos; fractal; particulate pollution

CONVECTION AND DIFFUSION ARE the two major mechanisms of mass transport for gas molecules and submicrometer aerosols in the pulmonary acinus. For gas transport, diffusion dominates at distances comparable to acinar size and over times comparable to breathing frequencies, and, therefore, theories based on diffusion are probably adequate. By contrast, the particle diffusivity of submicrometer-sized aerosols is very small, and, therefore, acinar convection, even though it is in a quasi-Stokes viscous flow regime (26), is correspondingly more important and may dominate aerosol transport. However, current theories describe aerosol transport as a dispersion (diffusion-like) process (e.g., Refs. 7, 10, 11, 19, 34). These theories are based on the following two key assumptions: *1*) acinar flow is basically kinematically reversible (i.e., during expiration each fluid particle retraces the path taken during inspiration) (9, 45), and *2*) all processes (including the coupling of Brownian diffusivity with the convective flow field and any kinematic irreversibility that may be present) that contribute to irreversible aerosol bolus spreading can be characterized as axial mixing with an effective longitudinal diffusivity (D_{eff}). The first assumption is based on classical fluid mechanics (36), and the second assumption is substantially equivalent to Taylor dispersion (35). As most aerosol studies are currently interpreted in the framework of these dispersion theories, experimental data are often reduced and analyzed through the use of some D_{eff} (e.g., Ref. 30), and many of the recent theoretical research efforts are focused on refining D_{eff} for better fit to experimental data, through which new insights into acinar transport mechanisms are sought (e.g., Ref. 6).

Our laboratory's recent findings (37–41), as well as those of others (8, 18), however, have questioned the validity of the basic assumptions that formed the basis of the dispersive theories. We have demonstrated that, because of the peculiar geometry of the alveolated duct and its time-dependent motion associated with tidal breathing, under certain conditions, alveolar flow can be chaotic (16, 40). As a consequence, acinar flow can be kinematically irreversible, even though it is a low-Reynolds number viscous flow, and lung expansion and contraction are approximately self-similar and reversible (1, 13, 14, 24, 46). These findings are supported by a discovery in fluid mechanics that chaotic mixing can occur even in a viscous flow (2, 25). We have also developed a theoretical analysis (5) to show that chaotic mixing is radically different from diffusive mixing. In chaotic acinar flow, a tracer bolus undergoes cyclic stretch-and-fold deformation, resulting in the induction of finer and finer scales in tracer profile with repeated breaths. This process soon reaches a critical moment at which the lateral distance between adjacent tracer striations becomes comparable to the diffusion distance. A burst of mixing occurs at this moment, and mixing is quickly completed.

The objectives of the studies reported here are, through numerical simulations of bolus experiments, to provide key data showing that the behavior of particles in a rhythmically expanding, multiply alveolated

Address for reprint requests and other correspondence: A. Tsuda, Physiology Program, Harvard School of Public Health, Huntington Ave., Boston, MA 02115 (E-mail: atsuda@hsph.harvard.edu).

The costs of publication of this article were defrayed in part by the payment of page charges. The article must therefore be hereby marked "*advertisement*" in accordance with 18 U.S.C. Section 1734 solely to indicate this fact.

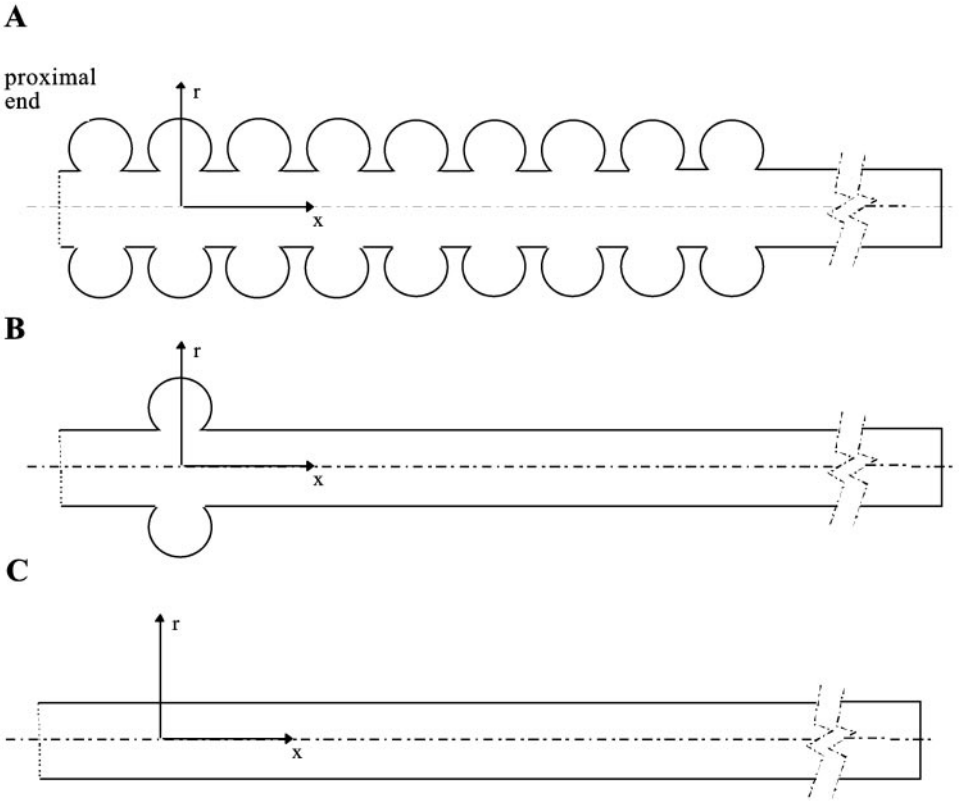

Fig. 1. Schematics of moving walled models. *A*: 9-cell alveolated duct model. *B*: isolated cell alveolated duct model. *C*: nonalveolated smooth-wall model.

duct flow, with a saddle point and associated vortexes in each air pocket, does not satisfy the fundamental assumptions of any dispersion theory and that the shape of a tracer bolus evolves to a stretch-and-fold fractallike pattern, similar to those found in flow visualization experiments in rat lungs (Tsuda A, Butler JP, and Rogers RA, unpublished observations). The results suggest that *1*) kinematic irreversibility is the origin of aerosol transport, *2*) axial transport cannot be characterizable by an effective diffusivity, and *3*) fractal trajectories can occur in most of the alveoli in the acinar tree. The alternative mechanism of aerosol transport that we propose here may, in fact, be the dominant mechanism determining deposition of submicrometer particles deep in the lung.

METHODS

In a previous investigation (40), we used the single-alveolus model to explore the basic physics operating in a viscous flow subjected to cyclic alveolar wall motion. The alveolus model used in the present investigation is also axisymmetric but comprises a central circular channel around which are placed nine tori, equispaced in the axial direction (Fig. 1*A*). Details of a typical cell are given in Fig. 2. The duct and alveolar walls move in a perfectly kinematically reversible, simple sinusoidal manner with a specific volume excursion C of 25% [$C = (V_{max} - V_{min})/V_{min}$, where V_{max} and V_{min} are the maximum and minimum volumes of the model, respectively] and a cycle period T of 3 s. These correspond roughly to typical tidal ventilation and respiratory period in human. Any length scale L of the model changes as $L(t) = \bar{L}[1 + K \sin(nt)]$, where $\bar{L}$ is the mean L value, t is time, $n = 2\pi/T$, and $K = (\phi - 1)/(\phi + 1)$, where $\phi = (1 + C)^{1/3}$. A smooth-walled, closed-end duct is fitted to the distal end of the model. The closed-end duct is used to approximate the airway distal of the site of interest up to the terminal alveoli, and it is also used to control the Reynolds number of the flow in the model.

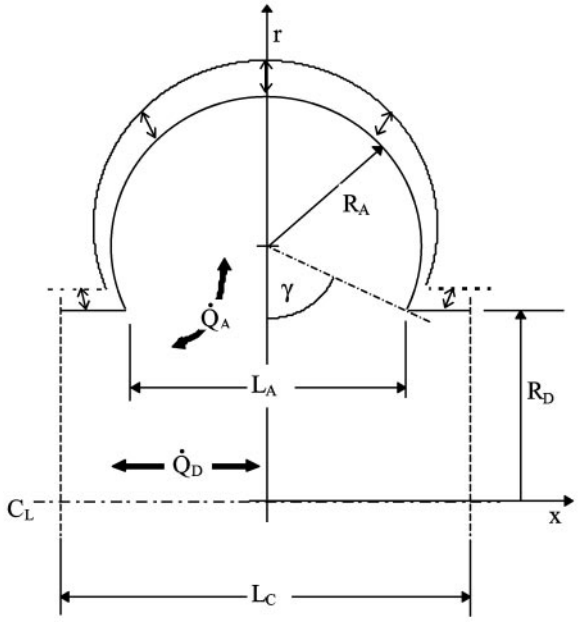

Fig. 2. Expanded view of a typical alveolar cell. R_D (= 250 μm), duct radius; R_A (= 200 μm), alveolar radius; L_A (= 346 μm), alveolar opening length; L_C (= 413 μm), alveolar cell length; $\dot{Q}_D$, ductal volume flow rate; $\dot{Q}_A$, alveolar volume flow rate; γ (= 60°), alveolar half-opening angle; C_L, duct center line. Note that the alveolar corners were rounded with the corner radius = 0.02 R_D.

The walls of this duct also move in the same sinusoidal manner as the main alveolus model. The mean length of this duct, $\bar{L}_D$, controls the bulk velocity U of the fluid entering the model; i.e., $U = \dot{Q}/\pi R_D^2 = 3nK\bar{L}_D \cos(nt)$, where $\dot{Q}$ is the volume flow rate and R_D is the duct radius. The root mean square (RMS) Reynolds number $Re_{RMS} = U_{RMS}\bar{R}_D/\nu$, where U_{RMS} is the RMS U and equals $U_{max}/\sqrt{2}$, where U_{max} is maximum U, $\bar{R}_D$ is the mean R_D, and ν is the kinematic viscosity. Re_{RMS} ranges from 0.006 to 0.728 in the alveolated region of the model. Using a closed-end duct has the added advantage of avoiding the difficulty of defining appropriate boundary conditions at the downstream boundary of the alveolated section. Typically, L_D/R_D is >100, and, hence, it can be assumed that the end of the closed-end duct was sufficiently far from the downstream boundary of the alveolated section so as not to affect the flow across this boundary adversely. As a further refinement to the original model, the sharp corner at the intersection between the alveolus and the duct is replaced by a more natural circular section. For comparative purposes, two other cases are also simulated. One is the flow in an isolated alveolus model (Fig. 1*B*), similar to that used in Tsuda et al. (40), and the other is the flow in a nonalveolated, rhythmically expanding straight tube (Fig. 1*C*).

The flow field is defined by the full, incompressible Navier-Stokes equations, which are solved numerically on a multiblock, body-fitted moving grid using the finite volume code CFX-4 (CFDS, AEA Technology, Harwell, UK). This general-purpose, pressure-correction code offers a variety of discretization schemes and solution techniques. In these calculations, central differencing is used to model the convection terms, and the implicit backward Euler method is used to advance the solution in time. A combination of the SIMPLEC pressure-correction method (44) and the Rhie-Chow (28) algorithm to eliminate pressure oscillations on the collocated gird (12) is used in the formulation of the discrete equations. Stone's method (33) is used to solve the discrete velocity equations, and the method of preconditioned conjugate gradients (see, for example, Ref. 22) is used to solve the discrete pressure correction equation. At the inlet, a constant-pressure boundary is defined. The value of the pressure on this boundary is set arbitrarily to zero, and, as for incompressible flow, only the pressure gradient is of importance. The no-slip condition is enforced on all solid surfaces, which, in the case of moving walls, means that the fluid matches the wall velocity at the fluid-wall interface. Tests were carried out to ensure that the solutions are grid independent and converged. For example, increasing the number of grid cells by 30% above that which was eventually used produces an increase of only 0.16% in the predicted maximum velocity. The final 73-block grid had a total of 38,349 active cells. With the use of a measure of error due to using backward Euler time stepping, suggested by Roache (29), a time step of $T/240$ is found to give sufficiently accurate results in that further reductions in the size of the time step used does not produce any significant reduction in the error. These simulations are computationally intensive, with one breathing cycle taking ~350 h on a Sun Ultra 10.

Particle trajectories are calculated in all three models using a special-purpose tracking routine. This routine reads a full cycle of flow field and grid data produced by CFX-4 and uses this data repeatedly, cycle after cycle, and a predictor and corrector method to track individual particles (fluid elements) over as many cycles as required. The time step used in the particle tracking routine is set independently of that for the flow-field solution. Before the particle track is advanced to the next time, the time step is recalculated, using local flow conditions, to ensure that the particle does not step out of the solution domain. At each particle-track time, a grid and flow field are created from the CFX-4 data using bicubic interpolation in space (27) and linear interpolation in time. For numerical efficiency, the routine solves the particle tracks in a stationary computational space, and, at each time step, the particle position is mapped back to physical space before it is written to an output file. The maximum error in the predicted particle position is estimated to be 0.2% of the distance traveled by the particle, and, in most cases, the error is considerably smaller than this.

RESULTS

Flow patterns. Solving the velocity field of the carrier gas on a moving grid over the physiologically relevant range of flow parameters ($Re_{RMS} < 1$) in a rhythmically expanding and contracting, multiply alveolated duct, we often detected the presence of slowly rotating recirculation in each alveolus (see Fig. 3, *A* and *B*). The size of the recirculation flow depends on the ratio between the alveolar flow ($\dot{Q}_A$) (i.e., flow produced by the volume change of the alveolus) and the volumetric ductal flow ($\dot{Q}_D$) ($\dot{Q}_A/\dot{Q}_D$). Similar to our previous study (40), we found that the smaller the $\dot{Q}_A/\dot{Q}_D$, the larger the alveolar recirculation. When $\dot{Q}_A/\dot{Q}_D$ is larger than ~0.1, however, the alveolar flow is largely radial without recirculation (Fig. 3*C*). Because, under normal breathing conditions or during moderate exercise, the value of $\dot{Q}_A/\dot{Q}_D$ is usually <0.05 in the majority of alveoli along the acinar tree (from the respiratory bronchioles to the last few generations) (37), we expect that most of the alveoli are likely to possess recirculation in their flow field. Importantly, the presence of alveolar recirculation in the cyclically expanding alveoli is topologically associated with the existence of a stagnation saddle point in each alveolar flow field (40), implying that chaotic mixing could originate in most of the alveoli (see DISCUSSION).

Interalveolar kinematic mixing. To demonstrate the effects of a series of saddle points on fluid flow irreversibility, the motion of massless particles was tracked over one ventilation cycle in a nine-cell alveolar model for three different ranges of $\dot{Q}_A/\dot{Q}_D$ ($0.0050 < \dot{Q}_A/\dot{Q}_D < 0.0053$, $0.040 < \dot{Q}_A/\dot{Q}_D < 0.069$, and $0.081 < \dot{Q}_A/\dot{Q}_D < 0.577$ shown in Fig. 4, *A*, *B*, and *C*, respectively). The particles were initially placed on radial lines across the duct midway between alveoli at three different initial axial locations (shown as three different colors, brown, green, and pink, in Fig. 4). As soon as inspiration begins, particles near the center line convect distally, proportionally to the bulk mean velocities (see $t/T = 0.25$ in Fig. 4). The lines of particles quickly approach each other and comigrate along the central channel, particularly in the cases of smaller $\dot{Q}_A/\dot{Q}_D$ (Fig. 4, *A* or *B*). The particles that were located initially near the alveolar opening enter the alveolus (Fig. 4). The depth of particle penetration into the alveolus during inspiration depends on the size of alveolar recirculation. When the alveolar recirculation is large (Fig. 4*A*), the particles penetrate deep into the alveoli, and the par-

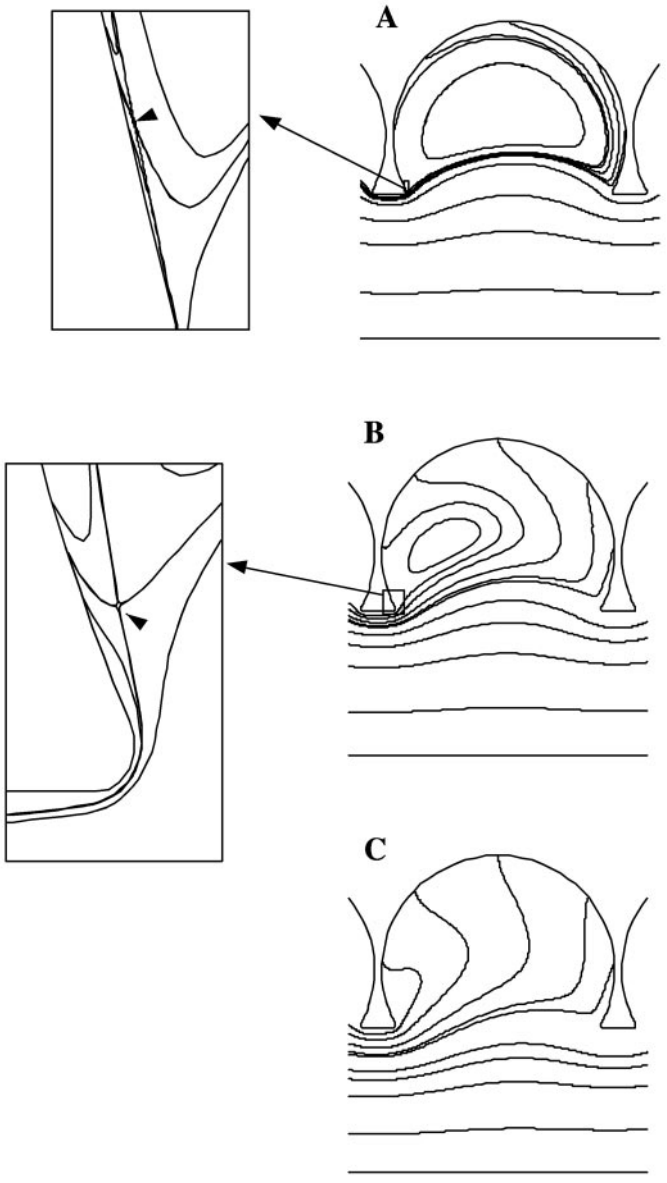

Fig. 3. Typical streamline patterns at the peak inspiration with various flow conditions. *A*: Reynolds number root mean square (Re_{RMS}) = 0.714, ratio of $\dot{Q}_A$ to $\dot{Q}_D$ ($\dot{Q}_A/\dot{Q}_D$) = 0.005. *B*: Re_{RMS} = 0.077, $\dot{Q}_A/\dot{Q}_D$ = 0.047. *C*: Re_{RMS} = 0.030, $\dot{Q}_A/\dot{Q}_D$ = 0.119. *Insets*: saddle points (arrowhead) near the proximal corner of alveoli.

ticles from the three different lines appear to be mixed during inspiration (see t/T = 0.25 and 0.5 in Fig. 4*A*).

As expiration starts, the particles start to move in a proximal direction. The reversibility of the particle motion is largely influenced by both the presence and the size of alveolar recirculation. When the alveolar recirculation is large (Fig. 4*A*), the particles exhibited three types of behavior. For type I, some particles, which were deep inside the alveolus at the end of inspiration, do not exit and remained trapped inside after expiration. For type II, particles that were inside the alveolus at the end of inspiration exit during expiration but do not come back to their original starting positions. For type III, particles near the center line that remained in the central channel during inspiration virtually retrace their inspiratory paths during expiration and thus arrive back very close to their original starting position. Comparing these three types of particle behavior, we notice that particles that were associated with alveolar recirculation (even for a short period of time) followed irreversible trajectories. When the alveolar recirculation is present but small (Fig. 4*B*), no particles are trapped in the alveolus, suggesting that the effects of small alveolar recirculation are insufficient to cause particle trapping. However, particles initially located near the side walls (which eventually became associated with alveolar recirculation) still display irreversible motion (type II). Particles that start near the channel center line come back to their original starting position (type III). In the complete absence of alveolar recirculation (Fig. 4*C*), the motion of all particles, even those that traveled inside the alveolus, is reversible.

For the purpose of comparison, the following two additional cases were also conducted: massless particles were tracked in a single-cell model and in an expandable straight-tube model (data not shown). Whereas the particles in the single-alveolus model, similar to the nine-cell alveolar model, exhibit some irreversibility, especially near the walls (type II), the particles in the expandable straight tube are reversible as predicted (42).

Motion of interface between inhaled tracer fluid and the host alveolar residual fluid. Regarding massless tracer particles as marked fluid elements, the interface between one fluid and another can be approximated by chords connecting initially adjacent particles (Fig. 5*A*). In our studies, this piecewise linear approximation to the interface can represent the front of incoming tidal gas or a tracer bolus facing the host alveolar residual gas. As we have demonstrated in Fig. 4, *A* and *B*, the kinematically irreversible deformation of the tracer interface seems to be due to its association with alveolar recirculation flow over the respiratory cycle. Thus characteristics (e.g., size and strength) of the alveolar recirculation may be major determinants in these processes. Our studies described here focus on the situation that presumably occurs deep in the acinus, where the alveolar flow exhibits a medium- to small-sized recirculation (Fig. 3*B*). Larger alveolar recirculation flow (Fig. 3*A*) is likely to occur near the entrance of acinus (e.g., respiratory bronchioles), and that case is discussed elsewhere (38).

To understand the temporal evolution of interface deformation (approximated as described above) in the case of flows with medium-sized alveolar recirculation, we monitored the motion of a tracer bolus for three cycles. In these simulations, we systematically increased the number of massless particles P ($P = 2^j$; where j = 3, 4, 5,. . .,13). For each P, the initial radial distribution of particles was adjusted in such a way that each particle represented equal cross-sectional annular area. Over each cycle, the interface progressively deforms into "fingerlike" protrusions located especially near the duct walls (Fig. 5*B*). Each protrusion

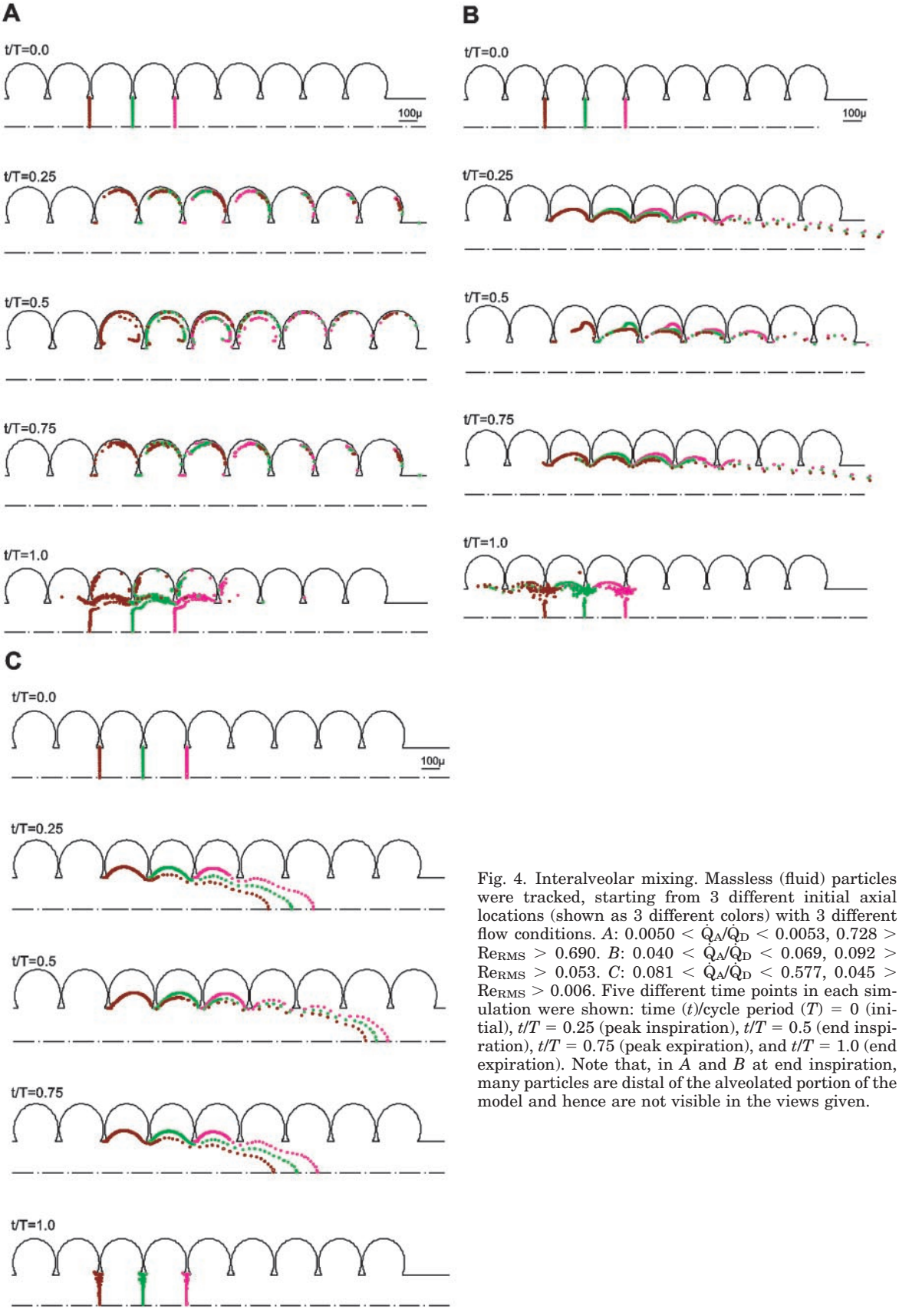

Fig. 4. Interalveolar mixing. Massless (fluid) particles were tracked, starting from 3 different initial axial locations (shown as 3 different colors) with 3 different flow conditions. *A*: $0.0050 < \dot{Q}_A/\dot{Q}_D < 0.0053$, $0.728 > Re_{RMS} > 0.690$. *B*: $0.040 < \dot{Q}_A/\dot{Q}_D < 0.069$, $0.092 > Re_{RMS} > 0.053$. *C*: $0.081 < \dot{Q}_A/\dot{Q}_D < 0.577$, $0.045 > Re_{RMS} > 0.006$. Five different time points in each simulation were shown: time (t)/cycle period (T) = 0 (initial), $t/T = 0.25$ (peak inspiration), $t/T = 0.5$ (end inspiration), $t/T = 0.75$ (peak expiration), and $t/T = 1.0$ (end expiration). Note that, in *A* and *B* at end inspiration, many particles are distal of the alveolated portion of the model and hence are not visible in the views given.

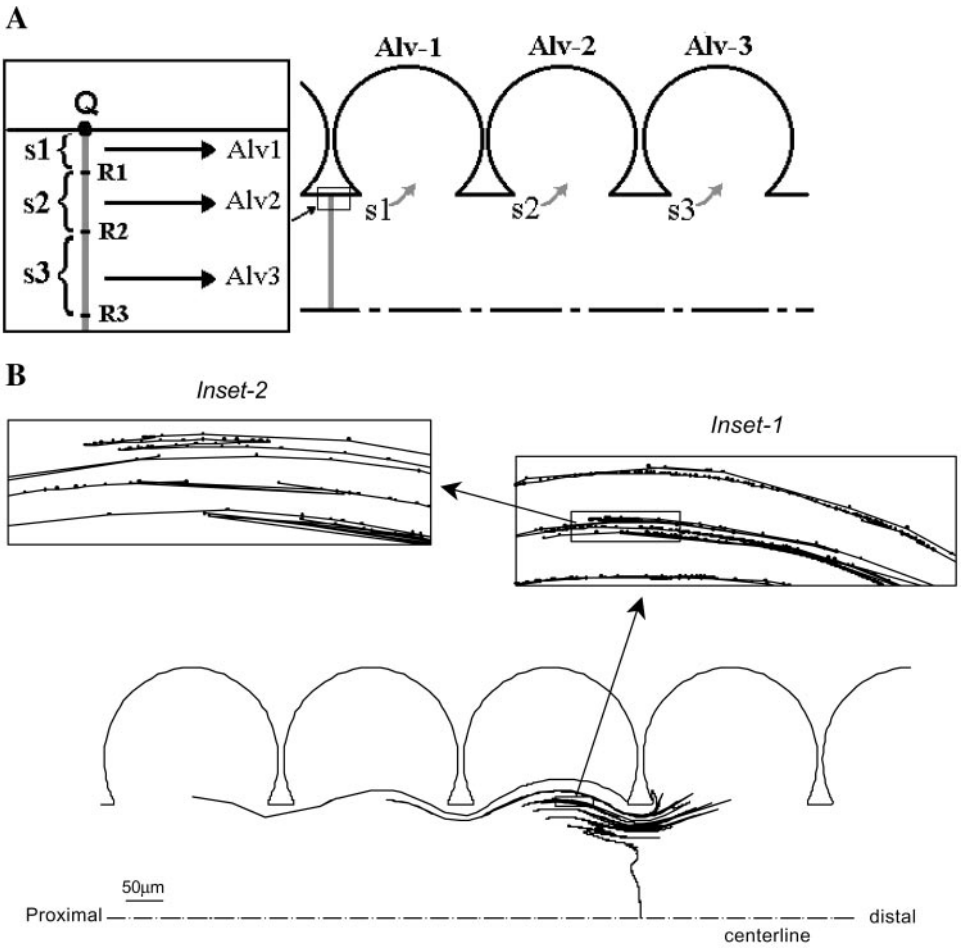

Fig. 5. Fluid interface between incoming air and alveolar residual gas. *A*: initial position of fluid interface shown by straight-line chords connecting initially adjacent particles. For definition of symbols Q, R1, R2, R3, s1, s2, s3, Alv-1, Alv-2, Alv-3, see DISCUSSION. *B*: the interface shows "fingerlike" protrusions at the end of the first cycle. *Inset 1*: each protrusion consists of complex stretched-and-folded patterns. *Inset 2*: similar and finer stretched-and-folded patterns appear as the scale becomes finer. Flow conditions in the 9-cell model: $0.040 < \dot{Q}_A/\dot{Q}_D < 0.069$, $0.092 > Re_{RMS} > 0.053$.

consists of complex stretched-and-folded patterns (Fig. 5*B*, *inset 1*), and, moreover, as the scale becomes finer, similar and finer stretched-and-folded patterns are revealed (Fig. 5*B*, *inset* 2). This suggests that the observed patterns might be qualitatively self-similar over a wide range of length scales. Such self-similarity is characteristic of fractal geometry observed in many chaotic systems (32).

To quantify the extent of stretch-and-fold flow irreversibility and especially to test whether axial spreading could be described by an effective diffusivity, we analyzed the shape of the tracer in axial and lateral directions separately. To characterize the axial phenomena, the axial variance (σ^2) of distribution of particles was computed and plotted vs. cycle number (N) as a family in the P employed (Fig. 6). The results show that σ^2 is independent of P and grows exponentially with increasing N [$\sigma^2 = 0.0474(e^{0.457N} - 1)$]. It is important to note that σ^2 does not increase linearly with N; this observation is fundamentally inconsistent with the predictions of the classical dispersion theory (discussed below).

To characterize the lateral phenomena, we examined the extent of tracer stretching [$\Delta L/L_o = (L - L_o)/L_o$, where L_o ($= \Sigma_{k=1}^{P}|x_{k+1} - x_k|$; x_k is the kth particle position) is the initial length of the tracer, and L ($=\Sigma_{k=1}^{P}|X_{k+1} - X_k|$; X_k is the kth particle's mapped

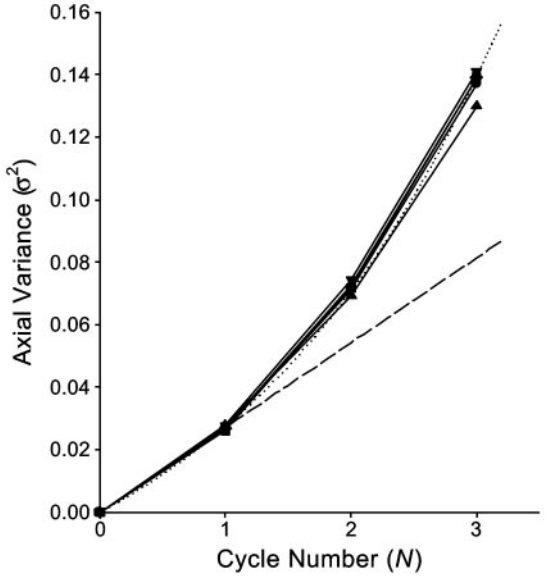

Fig. 6. Axial variance (σ^2) of particle distribution plotted vs. cycle number (N) as a family in the number of the particles (P). ▼, P = 512; ▲, P = 1,024; ■, P = 2,048; ◆, P = 4,098; ●, P = 8,192; dashed and dotted lines show linear growth ($\sigma^2 = 0.0271N$) and exponential growth [$\sigma^2 = 0.0474\ (e^{0.457N} - 1)$], respectively. Flow conditions in the 9-cell model: $0.040 < \dot{Q}_A/\dot{Q}_D < 0.069$, $0.092 > Re_{RMS} > 0.053$.

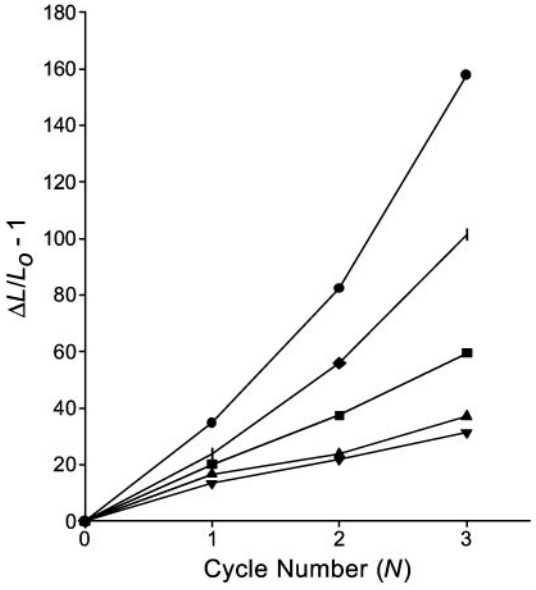

Fig. 7. Tracer stretching ($\Delta L/L_o$, where L is length and L_o is initial length) at end expiration plotted vs. N as a family in the P. ▼, P = 512; ▲, P = 1,024; ■, P = 2,048; ◆, P = 4,098; ●, P = 8,192. Flow conditions in the 9-cell model: $0.040 < \dot{Q}_A/\dot{Q}_D < 0.069$, $0.092 > Re_{RMS} > 0.053$.

position) is the tracer length at end expiration] and the pattern of the tracer. $\Delta L/L_o$ was plotted vs. N as a family in P (Fig. 7). The results show that the length of the tracer dramatically increases with increasing N and that this increase in $\Delta L/L_o$ is strongly depended on the P used to approximate the interface. (Note that this behavior is different from the axial phenomena in which the growth of σ^2 is essentially independent of the P.) Furthermore, the tracer length grows exponentially with N if a large P ($P > 4{,}096$) is used for simulation. Because the reciprocal of P is a parameter related to scale resolution in our simulation, the fact that the increase in $\Delta L/L_o$ with N strongly depends on P suggests that the resulting pattern of the tracer is fractal. To test this possibility, we examined the spatial pattern of all of the particles (~16,000) used for the simulation described above at the end of every cycle by employing the fractal analysis method of box-counting technique popularized by Glenny (15). Briefly, the test section of interest (usually the most particle-dense area) (Fig. 8, *inset*) was covered by M square boxes, each with an edge length E. Denoting the particle concentration in the ith box by μ_i and the overall mean concentration by $\bar{\mu}$, we computed the standard deviation [$SD^2 = \Sigma\,(\mu_i - \bar{\mu})^2/M$] and coefficient of variation, $CV = SD/\bar{\mu}$ of the set of concentrations μ_i. This procedure was repeated for box sizes spanning more than four orders of magnitude for the field of interest. A log-log plot of CV vs. E^2 reveals a linear relationship with slopes of −0.21, −0.25, and −0.25 for N = 1, 2, and 3, respectively (Fig. 8*B*). This indicates a power law relationship between the tracer particle distribution and the resolution of the analysis and that, therefore, the tracer pattern resulting from kinematically

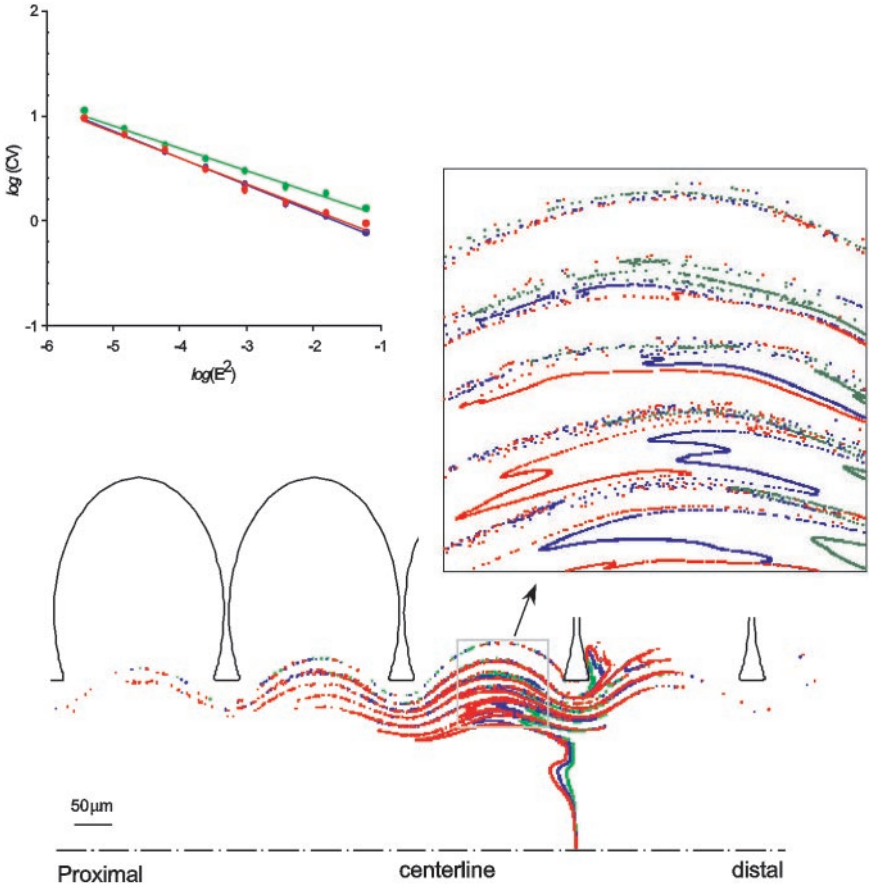

Fig. 8. *A*: distributions of massless (fluid) particles at N = 1 (green), N = 2 (blue), and N = 3 (red). Approximately 16,000 particles are shown for each N. *B*: box-counting analysis. A linear relationship on log[coefficient of variation (CV)] vs. log[edge length (E^2)] with a slope of −0.2 shows that the pattern of particle distribution is fractal with a fractal dimension $D \approx 1.2$. Flow conditions in the 9-cell model: $0.040 < \dot{Q}_A/\dot{Q}_D < 0.069$, $0.092 > Re_{RMS} > 0.053$.

irreversible acinar fluid mechanics may indeed be fractal with a fractal dimension $D \approx 1.2$ ($D = 1 -$ slope; Ref. 3). Remarkably, this dimension is close to that found in our animal experiments (unpublished observations, also see DISCUSSION).

DISCUSSION

The principal findings of this study are that *1*) chaotic fluid motion occurring in a rhythmically expanding and contracting, multiply alveolated duct induces substantial kinematic irreversibility in the acinus, even under low-Reynolds number flow conditions, and *2*) mixing due to this kinematic irreversibility is fundamentally different from the mixing described in dispersive processes.[1] A tracer (bolus) subjected to the chaotic flow field is deformed both axially and laterally. The σ^2 of particle distribution increases exponentially, rather than linearly, with increasing cycle time; thus axial bolus spreading does not obey the basic rules described in classical diffusive transport theories (35). The cycle-by-cycle evolution of lateral particle distribution is even more complex. The tracer forms fingerlike protrusions, even after one cycle. The tracer length exponentially increases as N increased, forming characteristic stretch-and-fold fractal-like patterns.

Chaotic mixing in the pulmonary acinus. Viscous flow has been considered kinematically reversible if the boundary motion is reversible (36, 45). In the mid-1980s, however, there was a breakthrough discovery in fluid mechanics, namely, that even Stokes flow can be kinematically irreversible if the structure of the flow is chaotic (2, 25). In the last several years, applying this new concept to respiratory fluid mechanics, our laboratory has been studying the role of chaotic flow phenomena in the experimentally observed, yet theoretically unexplained, convective mixing occurring in the lung periphery (5, 16, 37, 40). In our laboratory's previous numerical study (16, 40), we reported that chaotic flow and chaotic mixing can occur in the alveolated duct because of its peculiar geometry and time-dependent motion associated with tidal breathing. We found that acinar flow was often slowly rotating in the alveolar air pocket, and the velocity field near the alveolar opening was complex with a stagnation saddle point typical of chaotic flow structure. Performing Lagrangian fluid particle tracking, we further demonstrated that, in such a flow structure, the motion of fluid, $x(t)$, could be highly complex, irreversible, and unpredictable even though it was governed by simple deterministic equations [$x(t) = \int v(x,t)\mathrm{d}t$, $x(0) = x_o$, where $v(x,t)$ denotes Eulerian velocity field].

Our initial, numerical investigations performed in a simplified system with an isolated, single alveolus were aimed at discovering and understanding the basic physics operating in a rhythmically expanding alveolar flow (16, 40). These studies, however, did not address the cumulative effects of multiple alveoli (i.e., a series of saddle points) on the fate of inhaled aerosols. There are roughly 300 million alveoli in the human lung (~10,000 alveoli in each of ~30,000 acini) (17). This means that, in each acinus, the incoming tidal air may sample roughly 200 alveoli along a longitudinal pathway, from the entrance of an acinus to the terminal alveolar sac (here, we assume that alveoli are uniformly spaced in nine intra-acinar airway generations). As demonstrated in Figs. 3 and 4, a series of saddle points and associated vortexes in each air pocket, generated in a cyclically expanding, multiply alveolated duct, make the supposedly reversible low-Reynolds number acinar flow highly irreversible and can cause substantial interalveolar convective mixing.

In the context of flow irreversibilities associated with multiple saddle points, it is important to recognize that the estimates that we obtain in this work may significantly underestimate the importance of convective mixing. In particular, we have explicitly assumed and, therefore, constrained the flow field to be axisymmetric, which is to say that all azimuthal velocity components (i.e., the component in the direction perpendicular to the *r-z* plane) are zero. This would imply that the presence of a saddle point in the longitudinal section would be associated with a saddle "line" or "circle" around the ductal axis. Such a flow structure is not only highly unlikely but also would be expected to be unstable and to break into a separate sequence of saddle points. Any such failure to preserve axial symmetry would thus enhance whatever convective mixing is already associated with the axisymmetric alveolated geometry.

Fingerlike protrusion. In this study, a line of massless particles was introduced in the alveolated duct to represent a fluid-fluid interface (Figs. 4 and 5*A*). The behavior of this interface, such as its reversibility and irreversibility, changes in its shape and size and contains crucial information for understanding the mechanism of mixing between inhaled particles and alveolar residual gas. By tracking the motion of the tracer particles, we have followed the motion of this interface over several cycles. Because the boundary of this line, shown as the point Q in Fig. 5*A*, is stationary on the wall because of the no-slip condition, the line expands when the alveolar walls expand during inspiration, and the line also tends to contract when the walls contract during expiration. However, the reversibility of this process depended on the nature of the flow fields sampled during expansion and contraction. The segments of the line near the channel center line are enormously stretched axially (see Fig. 4) and sample mostly reversible Poiseuille-like ductal flow fields (Fig. 3). Consequently, the interfacial line near the center line also shows approximately reversible behavior (Fig. 5*B*). By contrast, the segments of the lines near the walls (e.g., *segments s1*, *s2*, and *s3* in Fig. 5*A*) sample a series of irreversible alveolar flow fields (e.g., Alv-1, Alv-2, and Alv-3, respectively, in Fig. 5*A*) and, consequently, do not return to their original positions (Fig. 5*B*). Each of these line segments, separated by points

[1] It is unlikely that the results on kinematic irreversibility in this paper are important to ventilation-perfusion matching, but a quantitative assessment of this remains open.

that sample approximately reversible flow fields between alveoli (e.g., R1, R2, and R3) basically form one finger after a cycle (Fig. 5*B*). The number of "fingers," therefore, roughly matches the number of alveoli distal to the initial position. Although, in the present computational model, the number of alveoli that the tracer samples is limited to six (due to computational constraints), in a real acinus, the inhaled bolus is expected to encounter a larger number of alveoli (~200) along the acinar longitudinal pathway. This implies that the acinar airways are likely to be filled with many longitudinal fingers after a few breathing cycles. This prediction has been confirmed experimentally in our laboratory's recent flow visualization studies performed in rat acini (39).

The size of each finger depended on its resident time in alveolar recirculation. The line segments that were closer to the side walls (e.g., s1 and s2) spent more time in recirculation (Alv-1 and Alv-2, respectively) and produced longer fingers. As the N increased, the tracer repeatedly encountered alveolar recirculation; the number of fingers rapidly increased, and they propagated toward the channel center line. This global evolution of the tracer pattern (i.e., rapid increase in the number of fingers, cycle-by-cycle lateral propagation), together with progressively finer scale tracer striations (discussed below in detail), are important observations because they indicate a substantial net enhancement of lateral particle transport for deposition.

Axial phenomena–a departure from the conventional dispersion theory. In current theories, aerosol transport in the pulmonary acinus is described as a dispersion (diffusion-like) process, and the mixing phenomena are couched in the language of a D_{eff}. The most important feature of this approach is that, in any process that is dispersive in the sense that it can be characterized by an effective diffusivity, the variance of a bolus asymptotically increases linearly in time (or N). Phrased differently, the variance is an additive function over time. The reduction of experimental data through the use of some D_{eff} has thus been the framework by which many aerosol studies have been conducted (e.g., Ref. 30). For instance, bolus spreading in the tracheobronchial tree is commonly characterized by the difference between the inhaled and exhaled variances (proportional to H^2, where H is the bolus width at half height), given by $\sqrt{H_{\text{exp}}^2 - H_{\text{insp}}^2}$, where H_{exp} is expiratory H and H_{insp} is inspiratory H (43). This numerical maneuver is clearly based on the underlying assumption of additivity of variances.

In sharp contrast to these ideas, the result of our numerical experiment does not obey this basic rule (Fig. 6). The σ^2 of bolus particle distribution grows faster than linearly in time, in contrast to the linear growth predicted by all theories that are characterized by a D_{eff}.[2] It is important to emphasize here that mixing of kinematic origin (e.g., chaotic flow in the acinus) has a fundamentally different nature from mixing described in dispersive mechanisms; thus it cannot be described by any D_{eff}.

Lateral phenomena (fractal patterns). The results of our study show that complex flow phenomena can occur in the lateral direction. Because of alveolar flow irreversibility, the tracer (i.e., a series of line segments, s1, s2, etc., in Fig. 5*A*) deforms at every cycle, forming fine characteristic stretch-and-fold striation patterns (see Fig. 5*B, insets*), on top of the global fingerlike protrusion (Fig. 5*B*). Consequently, an enormously large lateral diffusion surface (which is represented as a stretched tracer line in our study) evolves over every cycle, suggesting a substantial enhancement of lateral particle transport and subsequent deposition on the acinar walls. Interestingly, we found that exact estimation of tracer length L was not possible because L was strongly dependent on the number of particles forming the tracer (Fig. 7). At sufficiently fine scales (i.e., when the number of test particles used is sufficiently large), the apparent L of the tracer increases exponentially with increasing N.

The analysis of potentially fractal patterns by the well-known method of box counting (32) was employed. The analysis shows that the distribution of tracer particles evolve in a fractal-like manner, with $D \approx 1.2$. The fact that the tracer pattern exhibits fractal characteristics is not entirely surprising, because the origin of particle irreversibility is due to chaotic alveolar flow, and deterministic chaos often manifests a fractal geometry (23, 32). On the other hand, it is important and remarkable that the fingerlike protrusions (i.e., global pattern) found in these simulations are strikingly similar to those found in the longitudinal airway section of our experiments performed with rat lungs (39). Moreover, our initial finding that $D \approx 1.2$ obtained in finer scale stretch-and-fold striations in the present numerical study is close to $D \approx 1.1$ found in those rat experiments (unpublished observations) is encouraging. Although further detailed analyses will be necessary to determine the dependence of the fractal dimension (or indeed if the pattern remains fractal) on model parameters, these similarities suggest that our numerical simulation, although based on highly idealized assumptions, does, in fact, capture the essential features of the underlying mixing mechanism, namely, that low-Reynolds number chaotic flow in the acinus determines particle transport in the lung.

Physiological origins of mixing. Our laboratory has recently proposed two possible origins of "stretch-and-fold" kinematics in the pulmonary acinus: first, that

[2] In a recent theoretical study in fluid mechanics, Jones and Young (21) showed that the axial variance of tracer fluid elements in low-Reynolds number chaotic flow in a twisted pipe grows faster than linearly with time. They also pointed out that the resulting distribution of the tracer particles exhibited a fractal pattern (20). Experimentally, whether variances are in fact additive or not in real lungs, there do not appear to be any data on the growth of bolus variance as a function of breath number. [This point should not be confused with the observation that there is an essentially linear relationship between bolus width and volume of penetration in the bronchial tree (18)].

induced by a small departure (asynchrony) from kinematically reversible motion of alveolar walls (16, 41), and, second, that due to the presence of saddle points associated with alveolar recirculation flows in the acinar flow field (40). With respect to the first mechanism, Miki et al. (24) reported the presence of a small but consistent geometric hysteresis (i.e., temporal asynchrony) in lung expansion during normal tidal ventilation in live rabbits. By matching this degree of geometric hysteresis, we have generated physiologically realistic asynchrony in physical models (41) and computational models (16), which demonstrated that geometrical hysteresis, even if small, can produce stretch-and-fold patterns and, consequently, induce substantial acinar flow irreversibility. In a related work, Smaldone et al. (31), using gravitational sedimentation of aerosol particles to estimate mean linear intercepts, showed significant geometric hysteresis in excised lungs with large-volume excursions from minimal volume and interpreted their data in terms of respiratory unit recruitment and derecruitment. Those studies, however, being restricted to single-volume histories, did not address the issue of mixing during cyclic ventilation and so are not strictly comparable to the present work. Finally, flow/volume hysteresis (different flow magnitudes at isovolume points on inspiration and expiration) can lead to differences in the velocity profiles in the central airways; this, in turn, can cause a difference in aerosol deposition between inspiration and expiration (4).

In contrast to these studies, which focus primarily on differing geometric features between inspiration and expiration, in this paper we investigate the second mechanism mentioned above. We believe that the presence of saddle points may be an equally fundamental mixing mechanism responsible for convective mixing in the acinus. Note that such saddle point singularities do not exist in rigid wall models of acinar flow but, through their association with alveolar recirculation, are necessarily linked to the cyclic motion of the alveolar walls. To distinguish clearly this mechanism from the former one (caused by geometric hysteresis), we used only kinematically reversible wall motion in these studies. The present paper extends our previous work (40), which was restricted to a saddle point in a single alveolar space, by considering the effect of multiple saddle points in a multiply alveolated channel. In practice, we believe that both mechanisms, asynchrony and saddle points, coexist in the pulmonary acinus, mutually enhancing each other in producing stretch-and-fold mixing.

Significance and conclusions. It is well established that exposure to environmental aerosol pollutants is associated with health risks, ranging from mild to life threatening (47). The exposure and pathophysiological consequences are clearly linked by two independent and separate causal pathways: the exposure-dose relationship (i.e., given an aerosol concentration in the ambient air, what is the actual dose delivered to the lung) and the dose-response relationship (i.e., for a given deposited dose or burden, what is the biological consequence). Despite the large literature on exposure assessment methodologies as well as on the pathophysiological consequences of short- and long-term exposures, there is much less known about the mechanisms contributing to the first of these links, and much deposition and mixing data are inconsistent with previous theories of mixing deep in the lung. It is important, therefore, to identify new potential mechanisms that may dominate aerosol transport, even when boundary motion is approximately reversible. We argue in this paper that chaotic mixing is such a candidate. We have shown, through realistic numerical simulation of the low-Reynolds number alveolated duct flow (and by comparison with experimental results in rat lungs; unpublished observations), that the peculiar geometry of the alveolated duct structure within the pulmonary acinus and its cyclic motion during breathing can give rise to *1*) a chaotic type of mixing associated with the presence of saddle points, *2*) slow recirculatory flow within the alveoli, and *3*) stretching and folding of stream surfaces. These, in turn, can significantly increase mixing, especially laterally, and will also contribute to an increasing σ^2 (which increases faster than linearly with breath number, an observation that is inconsistent with any dispersal mechanism that can be characterized by an effective axial diffusivity). We suggest that chaotic mixing may be the dominant mechanism of aerosol transport and deposition deep in the lung.

This study was supported by National Heart, Lung, and Blood Institute Grants HL-47428 and HL-54885 and, in part, by Environmental Protection Agency Research Award R827353.

REFERENCES

1. **Ardila R, Horie T, and Hildebrandt J.** Macroscopic isotropy of lung expansion. *Respir Physiol* 20: 105–115, 1974.
2. **Aref H.** Stirring by chaotic advection. *J Fluid Mech* 143: 1–21, 1984.
3. **Bassingthwaighte JJ, Liebovitch LS, and West BJ.** *Fractal Physiology*. Oxford, UK: Oxford Univ. Press, 1994.
4. **Bennett WD and Smaldone GC.** Inspiratory vs. expiratory aerosol deposition in excised dog lungs. *J Aerosol Sci* 18: 49–57, 1987.
5. **Butler JP and Tsuda A.** Effect of convective stretching and folding on aerosol mixing deep in the lung, assessed by approximate entropy. *J Appl Physiol* 83: 800–809, 1997.
6. **Darquenne Brant P, Heyder J, and Paiva M.** Aerosol dispersion in human lung: comparison between numerical simulations and experiments for bolus tests. *J Appl Physiol* 83: 966–974, 1997.
7. **Darquenne C and Paiva M.** One-dimensional simulation of aerosol transport and deposition in the human lung. *J Appl Physiol* 77: 2889–2898, 1994.
8. **Darquenne C, West JB, and Prisk GK.** Deposition and dispersion of 1-μm aerosol boluses in the human lung: effect of micro- and hypergravity. *J Appl Physiol* 85: 1252–1259, 1998.
9. **Davies CN.** Breathing of half-micron aerosols. II. Interpretation of experimental results. *J Appl Physiol* 32: 601–611, 1972.
10. **Edwards DA.** A general theory of the macrotransport of nondeposition particles in the lung by convective dispersion. *J Aerosol Sci* 25: 543–565, 1994.
11. **Egan MJ, Nixon W, Robinson NI, James AC, and Phalen RF.** Inhaled aerosol transport and deposition calculations for the ICRP Task Group. *J Aerosol Sci* 20: 1305–1308, 1989.
12. **Ferziger JH and Peric M.** *Computational Methods for Fluid Dynamics*. Berlin: Springer-Verlag, 1996, p. 157.

13. **Gil J, Bachofen H, Gehr P, and Weibel ER.** Alveolar volume-surface area relation in air- and saline-filled lungs fixed by vascular perfusion. *J Appl Physiol* 45: 990–1001, 1979.
14. **Gil J and Weibel ER.** Morphological study of pressure-volume hysteresis in rat lungs fixed by vascular perfusion. *Respir Physiol* 15: 190–213, 1972.
15. **Glenny RW.** Heterogeneity in the lung: concepts and measurement. In: *Complexities in Structure and Function of the Lung*, edited by Hlastala MP and Robertson HT. New York: Dekker, 1999, chapt. 11, p. 571–609.
16. **Haber S, Butler JP, Brenner H, Emanuel I, and Tsuda A.** Flow field in self-similar expansion on a pulmonary alveolus during rhythmical breathing. *J Fluid Mech* 405: 243–268, 2000.
17. **Haefeli-Bleuer B and Weibel ER.** Morphometry of the human pulmonary acinus. *Anat Rec* 220: 401–414, 1988.
18. **Heyder J, Blanchard JD, Feldman HA, and Brain JD.** Convective mixing in human respiratory tract: estimates with aerosol boli. *J Appl Physiol* 64: 1273–1278, 1988.
19. **ICRP.** *Human Respiratory Tract Model for Radiological Protection: A Report of a Task Group of the International Commission on Radiological Protection. ICRP Publication 66, Annals of the ICRP.* New York: Pergamon, 1994.
20. **Jones SW, Thomas OM, and Aref H.** Chaotic advection by laminar flow in a twisted pipe. *J Fluid Mech* 209: 335–357, 1989.
21. **Jones SW and Young WR.** Shear dispersion and anomalous diffusion by chaotic advection. *J Fluid Mech* 280: 149–172, 1994.
22. **Kightley JR and Jones IP.** A comparison of conjugate-gradient preconditionings for 3-dimensional problems on a CRAY-1. *Comput Phys Commun* 37: 205–214, 1985.
23. **Mandelbrot BB.** *The Fractal Geometry of Nature.* San Francisco, CA: Freeman, 1982.
24. **Miki H, Butler JP, Rogers RA, and Lehr J.** Geometric hysteresis in pulmonary surface-to-volume ratio during tidal breathing. *J Appl Physiol* 75: 1630–1636, 1993.
25. **Ottino JM, Leong CW, Rising H, and Swanson PD.** Morphological structures produced by mixing in chaotic flows. *Nature* 333: 419–425, 1988.
26. **Pedley TJ, Schroter RC, and Sudlow MF.** *Bioengineering Aspects of the Lung*, edited by West JB. New York: Dekker, 1977, p. 163–265.
27. **Press WH, Teukolsky SA, Vetterling WT, and Flannery BP.** *Numerical Recipes in FORTRAN: The Art of Scientific Computing* (2nd ed.). Cambridge, UK: Cambridge Univ. Press, 1992, p. 118.
28. **Rhie CM and Chow WLA.** A numerical study of the turbulent flow past an airfoil with trailing edge separation. *AIAA Stud J* 21: 1525–1532, 1983.
29. **Roache PJ.** Quantification of uncertainty in computational fluid dynamics. *Annu Rev Fluid Mech* 29: 123–160, 1997.
30. **Rosenthal FS, Blanchard JD, and Anderson PJ.** Aerosol bolus dispersion and convective mixing in human and dog lungs and in physical models. *J Appl Physiol* 73: 862–873, 1992.
31. **Smaldone GC, Mitzner WW, and Itoh H.** The role of alveolar recruitment in lung inflation: influence on pressure-volume hysteresis. *J Appl Physiol* 55: 1321–1332, 1983.
32. **Sommerer JC.** Fractal tracer distributions in complicated surface flows: an application of random maps to fluid dynamics. *Physica D* 76: 85–98, 1994.
33. **Stone HL.** Iterative solutions of implicit approximations of multidimensional partial differential equations. *SIAM J Numer Anal* 5: 530–558, 1968.
34. **Taulbee DB and Yu CP.** A theory of aerosol deposition in the human respiratory tract. *J Appl Physiol* 38: 77–85, 1975.
35. **Taylor GI.** Dispersion of soluble matter in solvent flowing slowly through a tube. *Proc R Soc Lond A* 219: 186–203, 1953.
36. **Taylor GI.** *Low Reynolds Number Flow (*16-mm film). Newton, MA: Educational Services, 1960.
37. **Tippe A and Tsuda A.** Recirculating flow in an expanding alveolar model: experimental evidence of flow-induced mixing of aerosols in the pulmonary acinus. *J Aerosol Sci* 31: 979–986, 2000.
38. **Tsuda A, Butler JP, and Henry FS.** Particle trapping by alveolar recirculation flow in a rhythmically expanding pulmonary acinus (Abstract). *Am J Respir Crit Care Med* 103: A165, 2001.
39. **Tsuda A, Butler JP, Roberts J, Lai J, and Rogers RA.** Stretching-and-folding convective flow mixing in a rhythmically expanding pulmonary acinus (Abstract). *Ann Biomed Eng* 26: S49, 1998.
40. **Tsuda A, Henry FS, and Butler JP.** Chaotic mixing of alveolated duct flow in rhythmically expanding pulmonary acinus. *J Appl Physiol* 79: 1055–1063, 1995.
41. **Tsuda A, Otani Y, and Butler JP.** Acinar flow irreversibility caused by perturbations in reversible alveolar wall motion. *J Appl Physiol* 86: 977–984, 1999.
42. **Uchida S and Aoki H.** Unsteady flows in a semi-infinite contracting or expanding pipe. *J Fluid Mech* 82: 371–387, 1977.
43. **Ultman JS.** Gas transport in the conducting airways. In: *Gas Mixing and Distribution in the Lung*, edited by Engel LA and Paiva M. New York: Dekker, 1985, vol. 25, chapt. 3, p. 36–136. (Lung Biol. Health Dis. Ser.)
44. **Van Doormal JP and Raithby GD.** Enhancements of the SIMPLE method for predicting incompressible fluid flows. *Numer Heat Transfer B* 7: 147–163, 1984.
45. **Watson EJ.** Fluid flow in a model alveolar sac. *J Appl Physiol* 37: 249–251, 1974.
46. **Weibel ER.** Functional morphology of lung parenchyma. In: *Handbook of Physiology. The Respiratory System. Mechanics of Breathing.* Bethesda, MD: Am. Physiol. Soc., 1986, sect. 3, vol. III, pt. 1, chapt. 8, p. 89–111.
47. **Wilson R and Spengler JD.** *Particles in Our Air*. Boston, MA: Harvard Univ. Press, 1996.